THE JOURNAL OF NAVIGATION (2014), **67**, 776–790.
doi:10.1017/S0373463314000216

Closed-loop EKF-based Pulsar Navigation for Mars Explorer with Doppler Effects

Jin Liu[1,2], Jiancheng Fang[2], Xiaolin Ning[2], Jin Wu[1] and Zhiwei Kang[3]

[1](*College of Information Science and Engineering, Wuhan University of Science and Technology, Wuhan 430081, People's Republic of China*)
[2](*School of Instrumentation Science and Opto-electronics Engineering, Beihang University (BUAA), Beijing 100191, People's Republic of China*)
[3](*College of Information Science and Engineering, Hunan University, Changsha 410082, People's Republic of China*)
(E-mail: liujin@wust.edu.cn)

To eliminate the impact of the Doppler effects caused by the motion of the Mars explorer, a novel X-ray pulsar navigation method based on a closed-loop filter is proposed. In the pulsar signal observation period, the Doppler velocity predicted by the orbit dynamic model and the prior information is utilised to compensate the X-ray photon time-of-arrival (TOA). However, because of the error in prior information, there is a bias caused by the Doppler compensation in the pulse time-of-arrival. The pulse TOA bias and the Mars explorer's state estimation error are correlated, which results in the decline of the Kalman filter performance. To deal with this problem, we build the TOA measurement model with respect to the state estimation error, and utilise the closed-loop extended Kalman filter (EKF) as the navigation filter, where the predicted state error is adopted as the state estimation. The simulation results demonstrate the feasibility, real-timeliness and effectiveness of the proposed navigation method. The navigation method based on the closed-loop EKF using the measurement model with the Doppler effects is more accurate than the traditional one.

KEY WORDS

1. Navigation. 2. Doppler effects. 3. X-ray pulsar. 4. Mars explorer.

Submitted: 18 September 2013. Accepted: 27 February 2014. First published online: 24 March 2014.

1. INTRODUCTION. Currently, ground stations will support Mars explorer orbit determination. This navigation method is subject to navigation accuracy, real-timeliness, reliability and spreadability. It cannot fulfil the requirement of deep space exploration for high-accuracy and real-time navigation. Consequently autonomous navigation systems (Xiong et al., 2013), which need not communicate with ground stations, are highly attractive.

Traditional celestial navigation (Ning et al., 2011; 2012) is a commonly used autonomous navigation method, whose measurement is the angle subtended at the

explorer between the line of sight to the star and near celestial body. Its position accuracy declines with the increase of the distance between the explorer and the near celestial body. The distance between the Mars explorer and the near celestial body is so long that the positioning accuracy of this navigation method is very low in transfer orbit. Thus, this method is not suitable for the transfer orbit of deep space exploration. Asteroid-based navigation methods (Zhang et al., 2009; Xu et al., 2007) acquire navigation information by observing an asteroid when the explorer approaches the asteroid, but cannot obtain navigation information when the distance between the explorer and asteroid is very large. Therefore this method realizes high-accuracy positioning determination only for a small fraction of the whole transfer orbit.

X-ray pulsar navigation is a novel navigation method for deep space exploration. X-ray pulsars are rapidly rotating neutron stars, which can generate X-ray pulsed radiation. X-ray radiation signals can be collected by X-ray sensors placed on the explorer. After a period of observation usually lasting for several minutes, the stable X-ray pulse profile is acquired through the epoch folding (EF) procedure (Emadzadeh and Speyer, 2011a). A pulse time-of-arrival (TOA) can be obtained by comparing the observed pulse profile with the standard one (Liu et al., 2010; 2012). Since TOA accuracy is unrelated to the explorer's position, this navigation method can provide positioning information for the whole transfer orbit.

Many studies of X-ray pulsar navigation have assumed that the frequency of pulsar signals is known (Li and Ke, 2011; Emadzadeh and Speyer, 2011b; Rinauro et al., 2013), which is an important parameter in the epoch folding procedure. However, the Doppler effects caused by the motion of the explorer result in the distortion of integrated pulse profile of an X-ray pulsar. Consequently, the pulse TOA accuracy declines. As we know, the pulse TOA accuracy affects the position determination accuracy. Conversely, the distortion of an integrated pulse profile reflects the Doppler velocity. Thus, many scholars have estimated the explorer's velocity based on the pulse profile distortion. Golshan and Sheikh (2008) utilized the maximum-likelihood (ML) estimation method to determine the position and velocity. And the accuracy of the ML method approaches the Cramer-Rao lower bound (CRLB) (Ashby and Golshan, 2008). Zhang et al. (2011) gave the conception of the profile entropy and based on this, a phase and frequency estimation method for X-ray pulsar has been proposed. Fei et al. (2011a; 2011b) divided pulsar signals into two parts, taking their similarity as the objective function, and estimated the Doppler velocity by minimizing this objective function. Xie et al. (2012) defined a profile feature function to measure the integrated pulse profile distortion. According to the relationship between the function value and Doppler velocity, the Doppler velocity has been recognised by a search method. These Doppler velocity estimation methods' velocity accuracies are also high.

The strategy of those methods is to estimate the spacecraft velocity by means of minimizing the distortion of the pulse profile. In a pulsar observation period, pulsar photons are collected by an X-ray sensor and simultaneously folded based on pulse period. At this time, the pulsar navigation performance will not be affected when the runtime of the EF procedure is less than a pulsar observation period. But after a pulsar observation, the measurements including the pulse TOA and the Doppler velocity must be acquired quickly. Unfortunately, those Doppler velocity estimation methods are executed after the pulsar observation. What is worse, they have a high computational cost. The reason is that in those methods, a large number of pulsar signals (in the order of $10^6 \sim 10^7$) are folded with different pulse periods, even the runtime for an EF

https://doi.org/10.1017/S0373463314000216 Published online by Cambridge University Press

procedure with one pulse period is too high for the pulsar navigation system. From the above analysis, we can see that multiple EF procedures must be avoided.

In this paper, to eliminate the Doppler effects with a small computational cost, we develop a novel X-ray pulsar navigation system for the Mars explorer resistant against Doppler effects, which avoids multiple EF procedures. In the pulsar signal observation period, we utilise the prior information to compensate for the Doppler effects. However, an error inevitably exists in the prior information, which leads to the pulse TOA bias that arises from the Doppler compensation. It can be found that there is a correlation between the pulsar navigation measurement bias and the state estimation error. Based on this, a novel TOA measurement model is built with respect to the state estimation error. We develop a closed-loop extended Kalman filter (EKF) using this novel TOA model, which is robust to the measurement bias caused by the Doppler compensation.

This paper is organized into six sections. After the introduction, the orbit dynamic model for the Mars explorer and pulsar signal Doppler compensation method are outlined in Section 2. The novel X-ray pulsar navigation measurement model is in Section 3. The closed-loop EKF using the measurement model with the Doppler effects (closed-loop EKF-MMDE) is described in Section 4. The simulation results in Section 5 demonstrate the real-timeliness and accuracy of the presented method and conclusions are drawn in Section 6.

2. PULSAR SIGNAL DOPPLER COMPENSATION.

In order to illustrate, we define the TOA of an individual pulse as the sub-TOA, while the TOA obtained from the pulse integrated profile is defined as the pulse TOA.

To reduce the Doppler effects caused by the motion of a Mars explorer, the position, velocity and acceleration estimations obtained from the orbit dynamic model and prior knowledge can be utilised to compensate individual photon TOA from an X-ray pulsar. However an error inevitably exists in the prior information. Therefore there is a bias in the TOA measurement after the Doppler compensation.

In this section, we analyse the orbit dynamic model for the Mars explorer, and build the state predicted error model. The X-ray pulsar photon EF procedure based on Doppler compensation is then given. Finally, we show the effect of Doppler compensation on pulse TOA, and build the pulse TOA measurement bias model with respect to the Mars explorer's state estimation error.

2.1. *The analysis of orbit dynamic model for Mars explorer.*

The Sun-centred inertial Cartesian coordinate system (J2000.0) is selected. The orbit dynamic model for the Mars explorer is given as:

$$\begin{cases} \dot{x} = v_x \\ \dot{y} = v_y \\ \dot{z} = v_z \\ \dot{v}_x = -\mu_s \dfrac{x}{r_{ps}^3} - \mu_m \left[\dfrac{x - x_1}{r_{pm}^3} + \dfrac{x_1}{r_{sm}^3} \right] - \mu_e \left[\dfrac{x - x_2}{r_{pe}^3} + \dfrac{x_2}{r_{se}^3} \right] + \Delta F_x \\ \dot{v}_y = -\mu_s \dfrac{y}{r_{ps}^3} - \mu_m \left[\dfrac{y - y_1}{r_{pm}^3} + \dfrac{y_1}{r_{sm}^3} \right] - \mu_e \left[\dfrac{y - y_2}{r_{pe}^3} + \dfrac{y_2}{r_{se}^3} \right] + \Delta F_y \\ \dot{v}_z = -\mu_s \dfrac{z}{r_{ps}^3} - \mu_m \left[\dfrac{z - z_1}{r_{pm}^3} + \dfrac{z_1}{r_{sm}^3} \right] - \mu_e \left[\dfrac{z - z_2}{r_{pe}^3} + \dfrac{z_2}{r_{se}^3} \right] + \Delta F_z \end{cases} \tag{1}$$

https://doi.org/10.1017/S0373463314000216 Published online by Cambridge University Press

Equation (1) can be rewritten in the general state equation as

$$\dot{\boldsymbol{X}}(t) = f(\boldsymbol{X}, t) + \boldsymbol{\omega}(t) \tag{2}$$

where the state vector $\boldsymbol{X}=[x,\ y,\ z,\ v_x,\ v_y,\ v_z]^{\mathrm{T}}$. $\boldsymbol{r}=[x,\ y,\ z]$ and $\boldsymbol{v}=\lfloor v_x,\ v_y,\ v_z\rfloor$ are the Mars explorer position and velocity vectors, respectively. $\dot{\boldsymbol{X}}(t)$ is the derivative of $\boldsymbol{X}$. $[x_1,\ y_1,\ z_1]$ and $[x_2,\ y_2,\ z_2]$ are the position vectors of Mars and the Earth, respectively. $\mu_s,\ \mu_m,\ \mu_e$ are the gravitational constants of the Sun, Mars and Earth respectively, and their values are $1{\cdot}327\times10^{11}\ \mathrm{km^3/s^2}$, $3{\cdot}986\times10^{5}\ \mathrm{km^3/s^2}$, $4{\cdot}2828\times10^{4}\ \mathrm{km^3/s^2}$, respectively. $r_{ps}=\sqrt{x^2+y^2+z^2}$, $r_{pm}=\sqrt{(x-x_1)^2+(y-y_1)^2+(z-z_1)^2}$, $r_{pe}=\sqrt{(x-x_2)^2+(y-y_2)^2+(z-z_2)^2}$ are the distances from the Mars explorer to the Sun centre, the Mars centre and the Earth centre, respectively. $r_{sm}=\sqrt{x_1^2+y_1^2+z_1^2}$, $r_{se}=\sqrt{x_2^2+y_2^2+z_2^2}$ are the distances from the Sun centre to the Mars centre and the Earth centre respectively. $\boldsymbol{\omega}=[0,\ 0,\ 0,\ \Delta F_x,\ \Delta F_y,\ \Delta F_z]^{\mathrm{T}}$, where $\Delta F_x,\ \Delta F_y,\ \Delta F_z$ are the perturbation force considering sun-press and other planets.

We can obtain the discrete form of Equation (2) as:

$$\boldsymbol{X}_k = \boldsymbol{X}_{k-1} + f(\boldsymbol{X}_{k-1}, k-1)T + \boldsymbol{A}(\boldsymbol{X}_k) f(\boldsymbol{X}_{k-1}, k-1)\frac{T^2}{2} + \boldsymbol{\omega}_{k-1} \tag{3}$$

where

$$\boldsymbol{A}(\boldsymbol{X}_k) = \left.\frac{\partial f(\boldsymbol{X})}{\partial \boldsymbol{X}}\right|_{\boldsymbol{X}=\boldsymbol{X}_k} = [\boldsymbol{0}_{3\times3},\ \boldsymbol{I}_{3\times3};\ \boldsymbol{S}(\boldsymbol{X}_k),\ \boldsymbol{0}_{3\times3}] \tag{4}$$

$$\boldsymbol{S}_k = \left.\frac{\partial \dot{\boldsymbol{v}}}{\partial \boldsymbol{r}}\right|_{\boldsymbol{r}=\boldsymbol{r}_k} \tag{5}$$

The corresponding state predicted model is as follows:

$$\tilde{\boldsymbol{X}}_k = \tilde{\boldsymbol{X}}_{k-1} + f(\tilde{\boldsymbol{X}}_{k-1}, k-1)T + \boldsymbol{A}(\tilde{\boldsymbol{X}}_k) f(\tilde{\boldsymbol{X}}_{k-1}, k-1)\frac{T^2}{2} + \boldsymbol{\omega}_{k-1} \tag{6}$$

According to Equations (3) and (6), we can get the corresponding predicted error model as:

$$\delta\boldsymbol{X}_k = \delta\boldsymbol{X}_{k-1} + \boldsymbol{A}(\tilde{\boldsymbol{X}}_k)\delta\boldsymbol{X}_{k-1}T = \boldsymbol{\Phi}_k\delta\boldsymbol{X}_{k-1} \tag{7}$$

where

$$\delta\boldsymbol{X}_k = \boldsymbol{X}_k - \tilde{\boldsymbol{X}}_k \tag{8}$$

$$\boldsymbol{\Phi}_k = \boldsymbol{I}_{6\times6} + \boldsymbol{A}(\tilde{\boldsymbol{X}}_k) \tag{9}$$

2.2. *Epoch folding method based on Doppler compensation.* Since the pulsar signals are very weak, the EF method is commonly used to enhance the signal to noise ratio (SNR) of the pulse profile. The EF method (Emadzadeh and Speyer, 2011a; Sheikh et al., 2006) is as follows:

(1) The X-ray sensor records the time-of-arrival of each individual X-ray photon with respect to the system clock. During the total observation period, a large number of photons, N, will have their arrival times recorded.

https://doi.org/10.1017/S0373463314000216 Published online by Cambridge University Press

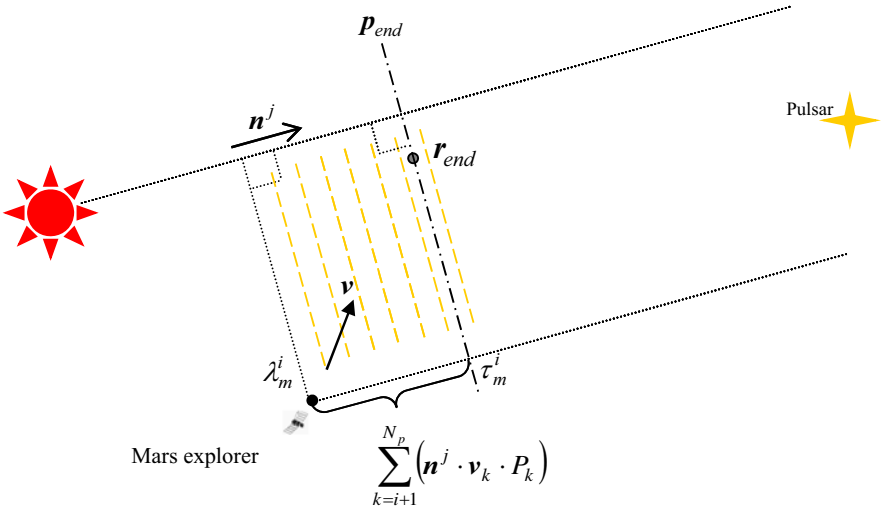

Figure 1. X-ray pulsar signal Doppler compensation.

(2) This set of photons is then folded at the predicted pulse period based on the known timing model of the pulsar. A binned pulse profile is then constructed by dividing the pulse phase into M equal bins and dropping each of the N photons into the appropriate phase bin.

After the EF procedure, converting time to phase of the pulse period, the TOA is then determined by measuring the phase offset of the observed profile with respect to the high SNR standard profile template. However, due to the motion of the Mars explorer, the pulsar signals TOA is subject to Doppler effects, so we must compensate for Doppler effects.

To reduce the computation load, we compensate the TOA of each X-ray photon with the pulse base. In order to illustrate conveniently, we define the TOA of individual pulse as sub-TOA, while the TOA obtained from the pulse integrated profile is defined as pulse TOA.

Suppose that the ith pulse period is P_i, the number of pulses in a pulsar observation period is N_p, $\boldsymbol{r}_{end}$ is defined as the explorer's position at the end of observation period, $\boldsymbol{n}^j$ is the line-of-sight direction of the jth pulsar, which may be considered constant throughout the solar system since the pulsars are so distant from the solar system. $\boldsymbol{p}_{end}$ is defined as the plane which passes through $\boldsymbol{r}_{end}$ and is perpendicular to $\boldsymbol{n}^j$, the TOA of mth X-ray photon in the ith pulse period at $\boldsymbol{p}_{end}$ and the explorer are τ^i_m and λ^i_m, respectively. Figure 1 presents the basic principle of pulsar signal Doppler compensation. As in the kth pulsar period, the Mars explorer moves $(\boldsymbol{n}^j)^{\mathrm{T}}\,\boldsymbol{v}_k\,P_k$ in the line-of-sight direction of the jth pulsar, the distance from the position of the Mars explorer at the ith pulse period to $\boldsymbol{p}_{end}$ is $\sum_{k=i+1}^{N_p}((\boldsymbol{n}^j)^{\mathrm{T}}\boldsymbol{v}_k P_k)$. Thus, the relationship of τ^i_m and λ^i_m can be expressed as:

$$\tau^i_m = \lambda^i_m - \sum_{k=i+1}^{N_p}\left(\frac{(\boldsymbol{n}^j)^{\mathrm{T}}\boldsymbol{v}_k P_k}{c}\right) \tag{10}$$

where v_i is the Mars explorer velocity in the ith pulse period. c is the speed of light.

https://doi.org/10.1017/S0373463314000216 Published online by Cambridge University Press

As the pulse profile of a pulse period consists of the photons in this pulse period, the compensation adopted by the pulse sub-TOA equals to that of X-ray photon in this pulse period. Suppose that the ith pulse sub-TOAs at $\boldsymbol{p}_{end}$ and the explorer are T_i and t_i, respectively. The relationship of T_i and t_i is

$$T_i = t_i - \sum_{k=i+1}^{N_p} \left(\frac{(\boldsymbol{n}^j)^{\mathrm{T}} \boldsymbol{v}_k P_k}{c} \right) \tag{11}$$

Using the orbit dynamic model, the velocity estimation and position estimation at the beginning of the pulsar observation period, we can predict the Mars explorer's velocity in the ith pulse period, $\hat{\boldsymbol{v}}_i$, and compensate the pulse sub-time-of-arrival with this predicted velocity. The compensated TOA of mth X-ray photon in the ith pulse period at $\boldsymbol{p}_{end}$ is $\hat{\tau}_m^i$:

$$\hat{\tau}_m^i = \lambda_m^i - \sum_{k=i+1}^{N_p} \left(\frac{(\boldsymbol{n}^j)^{\mathrm{T}} \hat{\boldsymbol{v}}_k P_k}{c} \right) \tag{12}$$

Correspondingly, the ith pulse compensated sub-TOA at $\boldsymbol{p}_{end}$, $\hat{T}_i$ can be expressed as:

$$\hat{T}_i = t_i - \sum_{k=i+1}^{N_p} \left(\frac{(\boldsymbol{n}^j)^{\mathrm{T}} \hat{\boldsymbol{v}}_k P_k}{c} \right) \tag{13}$$

The EF method based on Doppler compensation is summarised as follows:

(1) The sensor records the time-of-arrival of each individual X-ray photon.
(2) The time of arrival of each individual X-ray photon is corrected by Equation (12). $\hat{\boldsymbol{v}}_i$ in Equation (12) can be calculated by the fourth-order Runge-Kutta method and the transfer orbit dynamic model.
(3) This set of photons is then folded at the predicted pulse period based on the known timing model of the pulsar. A binned pulse profile is then constructed by dividing the pulse phase into M equal bins and dropping each of the N photons into the appropriate phase bin.

2.3. *TOA bias model.* In the EF method based on Doppler compensation, the velocity prediction error affects sub-TOA accuracy. Next, we analyse this effect.

Suppose that the velocity error in the ith pulse period of the kth pulsar observation period, $\Delta \boldsymbol{v}_i$, is

$$\begin{aligned} \Delta \boldsymbol{v}_i &= \boldsymbol{v}_i - \hat{\boldsymbol{v}}_i \approx [\boldsymbol{0}_{3\times 3} \ \boldsymbol{I}_{3\times 3}](\boldsymbol{I}_{6\times 6} + \boldsymbol{A}(\tilde{\boldsymbol{X}}_{k-1}) \cdot i \cdot P_0)\delta \boldsymbol{X}_{k-1} \\ &= [\boldsymbol{S}_{k-1} \cdot i \cdot P_0, \ \boldsymbol{I}_{3\times 3}]\delta \boldsymbol{X}_{k-1} \end{aligned} \tag{14}$$

Then, the pulse sub-TOA compensation error of the ith pulse period, $\Delta \hat{T}_i$, is:

$$\begin{aligned} \Delta T_i &= T_i - \hat{T}_i \\ &= -\sum_{k=i+1}^{N_p} \frac{(\boldsymbol{n}^j)^{\mathrm{T}} \Delta \boldsymbol{v}_k}{c} P_0 \\ &= -\frac{P_0}{c} (\boldsymbol{n}^j)^{\mathrm{T}} \left[\boldsymbol{S}_{k-1} \cdot \frac{N_p(N_p+1) - i(i+1)}{2} \cdot P_0, \ (N_p - i) \, \boldsymbol{I}_{3\times 3} \right] \delta \boldsymbol{X}_{k-1} \end{aligned} \tag{15}$$

https://doi.org/10.1017/S0373463314000216 Published online by Cambridge University Press

As the pulsar profile is integrated with all pulses in the whole pulsar signal observation period, the pulse TOA estimation bias equals the mean of pulse time-of-arrival compensation error of all periods. The pulse TOA bias can be expressed as:

$$\beta_k^j = \frac{1}{N_p}\sum_{i=1}^{N_p}\Delta\hat{T}_i = -\frac{(\boldsymbol{n}^j)^{\mathrm{T}}}{c}\left[\frac{T^2}{3}\boldsymbol{S}_{k-1},\ \ \frac{T}{2}\boldsymbol{I}_{3\times 3}\right]\delta\boldsymbol{X}_{k-1} \tag{16}$$

where the observation period $T = N_p P_0$. We can see that this bias is correlated with the velocity estimation error $\Delta\boldsymbol{v}$.

Therefore Equation (16) is the pulse TOA measurement bias model with respect to the state estimation error.

3. X-RAY PULSAR NAVIGATION MEASUREMENT.

An X-ray pulsar measurement is the difference between the pulse TOAs observed by the X-ray sensor at the Mars explorer and predicted by the pulse-timing model at SSB (solar system barycentre) (Liu et al., 2010; 2012). t^j and t_b^j are the pulse TOAs of the jth pulsar at the Mars explorer and at the SSB respectively. $\boldsymbol{n}^j$ is the line-of-sight direction vector of the jth pulsar, which may be considered constant throughout the solar system since the pulsars are so distant from the Solar system. $\boldsymbol{r}$ is the position vector of the Mars explorer with respect to the SSB. c is the speed of light. The offset $t_b{}^j - t^j$ reflects $\boldsymbol{r}$'s projection on $\boldsymbol{n}^j$. The offset to the first order is

$$t_b^j - t^j = \frac{1}{c}(\boldsymbol{n}^j)^{\mathrm{T}}\boldsymbol{r} \tag{17}$$

Considering the relativistic effects, geometric effects and TOA measurement bias, the time transfer model can be expressed as:

$$\begin{aligned} t_b^j - (t^j - \beta^j) = {} & \frac{1}{c}(\boldsymbol{n}^j)^{\mathrm{T}}\boldsymbol{r} + \frac{1}{2cD_0^j}\left[-|\boldsymbol{r}|^2 + ((\boldsymbol{n}^j)^{\mathrm{T}}\boldsymbol{r})^2 - 2\boldsymbol{b}^{\mathrm{T}}\boldsymbol{r} + 2(\boldsymbol{b}^{\mathrm{T}}\boldsymbol{r})((\boldsymbol{n}^j)^{\mathrm{T}}\boldsymbol{r})\right] \\ & + \frac{2\mu_{Sun}}{c^3}\ln\left|\frac{(\boldsymbol{n}^j)^{\mathrm{T}}\boldsymbol{r} + |\boldsymbol{r}|}{(\boldsymbol{n}^j)^{\mathrm{T}}\boldsymbol{b} + |\boldsymbol{b}|} + 1\right| \end{aligned} \tag{18}$$

where D_0^j is the range from the jth pulsar to the SSB, $\boldsymbol{b}$ is the position of the SSB relative to the Sun, μ_{Sun} is the gravitational constant of the Sun. The second and third terms on the right-hand side of Equation (18) are referred to as Roemer delay. The fourth term is the Shapiro delay effect. Equation (18) can be also represented as:

$$\begin{aligned} c(t_b^j - t^j) = {} & (\boldsymbol{n}^j)^{\mathrm{T}}\boldsymbol{r} + \frac{1}{2D_0^j}[-|\boldsymbol{r}|^2 + ((\boldsymbol{n}^j)^{\mathrm{T}}\boldsymbol{r})^2 - 2\boldsymbol{b}^{\mathrm{T}}\boldsymbol{r} + 2(\boldsymbol{b}^{\mathrm{T}}\boldsymbol{r})((\boldsymbol{n}^j)^{\mathrm{T}}\boldsymbol{r})] \\ & + \frac{2\mu_{Sun}}{c^2}\ln\left|\frac{(\boldsymbol{n}^j)^{\mathrm{T}}\boldsymbol{r} + |\boldsymbol{r}|}{(\boldsymbol{n}^j)^{\mathrm{T}}\boldsymbol{b} + |\boldsymbol{b}|} + 1\right| - c\beta^j \end{aligned} \tag{19}$$

Suppose that the TOA measurement $\boldsymbol{Y}_k = [c(t_b^1 - t^1),\ c(t_b^2 - t^2),\ \ldots,\ c(t_b{}^{num} - t^{num})]$ and measurement noise $\boldsymbol{\xi} = [\varsigma^1,\ \varsigma^2,\ \ldots,\ \varsigma^{num}]^{\mathrm{T}}$, where $c(t_b{}^j - t^j)$ and ς^j are the measurement and noise of the jth pulsar respectively, *num* is the number of the

https://doi.org/10.1017/S0373463314000216 Published online by Cambridge University Press

adopted pulsars. The measurement model can be presented as:

$$\boldsymbol{Y}_k = h(\boldsymbol{X}_k, k) + \boldsymbol{B}_k + \boldsymbol{\xi}_k \tag{20}$$

where the TOA bias matrix $\boldsymbol{B}_k$ can be expressed as:

$$\begin{aligned}\boldsymbol{B}_k &= [-c\beta_k^1, -c\beta_k^2, \ldots, -c\beta_k^{num}] = \boldsymbol{n}^T \left[\frac{T^2}{3}\boldsymbol{S}_k, \frac{T}{2}\boldsymbol{I}\right]\delta\boldsymbol{X}_{k-1} \\ &= \boldsymbol{n}^T \left[\frac{5T^2}{6}\boldsymbol{S}_k, \frac{T}{2}\boldsymbol{I} + \frac{T^3}{3}\boldsymbol{S}_k\right]\delta\boldsymbol{X}_{k-1}\end{aligned} \tag{21}$$

where

$$\boldsymbol{n} = [\boldsymbol{n}^1, \boldsymbol{n}^2, \ldots, \boldsymbol{n}^{num}] \tag{22}$$

$h(\boldsymbol{X}_k, k) = [h^1(\boldsymbol{X}_k, k), h^2(\boldsymbol{X}_k, k), \ldots h^{num}(\boldsymbol{X}_k, k)]^{\mathrm{T}}$, $h^j(\boldsymbol{X}_k, k)$ is the measurement equation of the jth pulsar, and can be expressed as:

$$\begin{aligned}h^j(\boldsymbol{X}_k, k) &= (\boldsymbol{n}^j)^{\mathrm{T}}\boldsymbol{r} + \frac{1}{2D_0^j}[-|\boldsymbol{r}|^2 + ((\boldsymbol{n}^j)^{\mathrm{T}}\boldsymbol{r})^2 - 2\boldsymbol{b}^{\mathrm{T}}\boldsymbol{r} + 2(\boldsymbol{b}^{\mathrm{T}}\boldsymbol{r})((\boldsymbol{n}^j)^{\mathrm{T}}\boldsymbol{r})] \\ &\quad + \frac{2\mu_{Sun}}{c^2}\ln\left|\frac{(\boldsymbol{n}^j)^{\mathrm{T}}\boldsymbol{r} + |\boldsymbol{r}|}{(\boldsymbol{n}^j)^{\mathrm{T}}\boldsymbol{b} + |\boldsymbol{b}|} + 1\right|\end{aligned} \tag{23}$$

where $j = 1, 2, \ldots, num$.

It is important to determine the pulse TOA with an accuracy that is determined by the SNR of the profile and not by the time resolution. The method given by Taylor (Xie et al., 2012) is independent of time resolution, where a pulse TOA is generated by comparing an observed profile with high SNR standard template profile. The standard variance σ^j of ς^j can be calculated as follows (Sheikh et al., 2006):

$$\sigma^j = \frac{Wc\sqrt{[B_X + F_X(1 - p_f)]d + F_X p_f}}{2F_X\sqrt{ATp_f}} \tag{24}$$

where B_X is the X-ray background radiation flux, F_X is the radiation photon flux from X-ray pulsar, p_f is the ratio of the pulse radiation flux to the average radiation flux in a pulse period, A is the area of the X-ray sensor, T is the pulsar signals observation period, W is the width of the pulse, d is the ratio of the pulse width to the pulse period, c is the speed of light.

4. CLOSED-LOOP EKF.

Considering the fact that the TOA measurement is related with the state error, we adopt the closed-loop EKF (Qiao et al., 2010), where the state predicted error is utilised as the novel state estimation.

Suppose that we have a system given by

$$\delta\boldsymbol{X}_k = \boldsymbol{\Phi}_k\delta\boldsymbol{X}_{k-1} + \boldsymbol{\omega}_{k-1} \tag{25}$$

$$\delta\boldsymbol{Y}_k = \boldsymbol{H}_k\delta\boldsymbol{X}_k + \boldsymbol{\delta}_k \tag{26}$$

https://doi.org/10.1017/S0373463314000216 Published online by Cambridge University Press

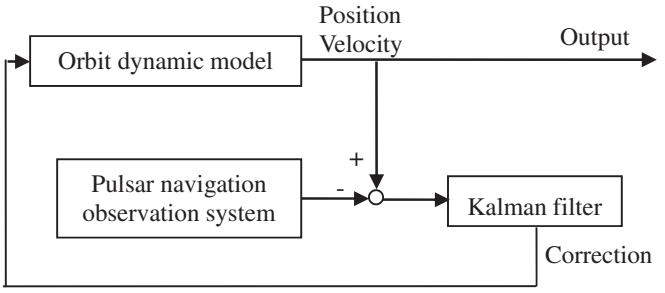

Figure 2. Principle of closed-loop correction.

The error measurement considering the Doppler effects, $\delta \boldsymbol{Y}_k$, can be expressed as:

$$\begin{aligned}\delta \boldsymbol{Y}_k &= \boldsymbol{Y}_k - h(\tilde{\boldsymbol{X}}_k, k) \\ &= [\boldsymbol{n},\ \boldsymbol{0}_{3\times 3}]\delta \boldsymbol{X}_k + \boldsymbol{B} + \boldsymbol{\xi} \\ &= \boldsymbol{n}^{\mathrm{T}}\left[\boldsymbol{I}_{3\times 3} + \frac{5T^2}{6}\boldsymbol{S}_{k-1},\ \ \frac{T}{2}\boldsymbol{I}_{3\times 3} + \frac{T^3}{3}\boldsymbol{S}_{k-1}\right]\delta \boldsymbol{X}_k + \boldsymbol{\xi} \\ &= \boldsymbol{H}_k \delta \boldsymbol{X}_k + \boldsymbol{\xi}\end{aligned} \tag{27}$$

where

$$\boldsymbol{H}_k = \boldsymbol{n}^{\mathrm{T}}\left[\boldsymbol{I}_{3\times 3} + \frac{5T^2}{6}\boldsymbol{S}_{k-1},\ \ \frac{T}{2}\boldsymbol{I}_{3\times 3} + \frac{T^3}{3}\boldsymbol{S}_{k-1}\right] \tag{28}$$

When the spacecraft is in the transfer orbit, the value of $\boldsymbol{S}$ is very large. In this condition, we can adopt the simplified measurement matrix as:

$$\boldsymbol{H}_k = \boldsymbol{n}^{\mathrm{T}}\left[\boldsymbol{I}_{3\times 3},\ \ \frac{T}{2}\boldsymbol{I}_{3\times 3}\right] \tag{29}$$

Equation (27) is the measurement model with the Doppler effects.

The principle of the closed-loop correction filter is shown in Figure 2. The equations for the closed-loop extended Kalman filter are shown as:

$$\boldsymbol{P}_k^- = \boldsymbol{\Phi}_{k-1}\boldsymbol{P}_{k-1}^+\boldsymbol{\Phi}_{k-1}^T + \boldsymbol{Q}_{k-1} \tag{30}$$

$$\boldsymbol{K}_k = (\boldsymbol{P}_k^- \boldsymbol{H}_k^{\mathrm{T}})(\boldsymbol{H}_k \boldsymbol{P}_k^- \boldsymbol{H}_k^{\mathrm{T}} + \boldsymbol{R}_k)^{-1} \tag{31}$$

$$\delta \boldsymbol{X}_k = \boldsymbol{K}_k \delta \boldsymbol{Y}_k \tag{32}$$

$$\boldsymbol{P}_k^+ = \boldsymbol{P}_k^- - \boldsymbol{K}_k \boldsymbol{H}_k \boldsymbol{P}_k^- \tag{33}$$

$$\boldsymbol{X}_k^+ = \boldsymbol{X}_k^- + \delta \boldsymbol{X}_k \tag{34}$$

5. SIMULATION RESULTS. In order to demonstrate the feasibility and effectiveness of the proposed navigation system, we show the simulation results in this section. The simulation conditions are shown as follows.

We adopt two orbits: (a) The orbit of the American Mars Pathfinder, which launched on 4 December 1996 at 06:58:10·00 UT. The initial orbit elements of the American Mars Pathfinder are shown in Table 1. The simulation time is from

https://doi.org/10.1017/S0373463314000216 Published online by Cambridge University Press

Table 1. Initial orbital elements of the American Mars Pathfinder.

Orbital element	Value
Semi-major Axis	193216365·381 km
Eccentricity	0·236386
Inclination	23·455°
Right Ascension of Ascending Node	0·258°
Argument of Periapsis	71·347°
True Anomaly	85·152°

Table 2. Initial orbital elements of the Mars satellite.

Orbital element	Value
Semimajor Axis	6794 km
Eccentricity	0
Inclination	45°
Right Ascension of Ascending Node	0°
Argument of Periapsis	0°
True Anomaly	0°

Table 3. Parameters of pulsars.

Pulsar	B0531 + 21	B1821–24	B1937 + 21
Right ascension angle/°	83·63	276·13	294·92
Declination angle/°	22·01	− 24·87	21·58
D_0/kpc	2·0	5·5	3·6
P/s	0·0334	0·00305	0·00156
W/s	$1{\cdot}7\times10^{-3}$	$5{\cdot}5\times10^{-5}$	$2{\cdot}1\times10^{-5}$
F_x(ph/cm^2/s)	1·54	$1{\cdot}93\times10^{-4}$	$4{\cdot}99\times10^{-5}$
P_f/%	70	98	86

1 Mar 1997 00:00:00·00 UT to 2 Mar 1997 00:00:00·00 UT. (b) The orbit of the Mars satellite, whose initial orbit elements are shown in Table 2. The simulation time is 10 days. The two orbits of the Mars explorer are simulated with the Satellite Tool Kit (STK), which takes the perturbation effects into account.

The measurement noise standard covariance of the jth pulsar can be calculated as Equation (24). The X-ray background radiation flux is assumed as 0·005 ph/cm^2/s. That value was chosen based on the empirical research done at the Naval Research Laboratory (Dennis, 2005). The area of the X-ray sensor is 1 m^2. The creation of a catalogue of pulsars is most useful for deep space navigation. In this paper, three commonly used pulsars, whose figures of merit are highest in all pulsars, are adopted, and the parameters of those pulsars are shown as Table 3.

The other parameters of the filter are shown as Table 4. The experiments were carried out on an Acer TravelMate 8572 TG Notebook with a CPU clock rate of 2·4 GHz and a memory of 2 GB.

https://doi.org/10.1017/S0373463314000216 Published online by Cambridge University Press

Table 4. Parameters of navigation filter.

Parameter	Value
Number of X-ray sensors	1
Sampling period (the observation period)	1000 s
Initial state errors	$\delta \boldsymbol{X}(0) = [6000\text{ m}, 6000\text{ m}, 6000\text{ m}, 20\text{ m/s}, 20\text{ m/s}, 15\text{ m/s}]$
Initial estimation error covariance	$\boldsymbol{P}(0)$ is selected at random
State process noise covariance	$\boldsymbol{Q} = diag[q_1^2, q_1^2, q_1^2, q_2^2, q_2^2, q_2^2]$, where $q_1 = 4$ m $q_2 = 6 \times 10^{-4}$ m/s for transfer orbit; $q_1 = 20$ m $q_2 = 0{\cdot}13$ m/s for satellite orbit.

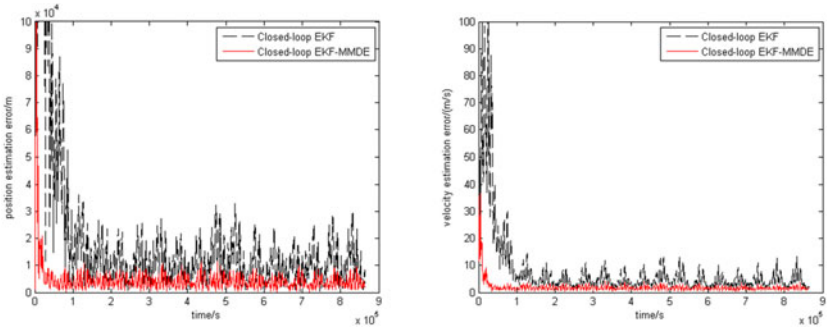

(a) Position estimation error (b) Velocity estimation error

Figure 3. Estimation error of the two navigation methods.

5.1. *Mars satellite obit*. We investigate the performance of closed-loop EKF-MMDE and the traditional closed-loop EKF. Figure 3 shows the performance comparison of these two navigation methods using the same simulation conditions described above. As the results in Figure 3 demonstrate, the two methods can converge very well for a Mars probe orbit, and the closed-loop EKF-MMDE performs considerably better. Table 5 shows the comparison between the traditional closed-loop EKF and the closed-loop EKF-MMDE over 100 Montè-Carlo trials. It can be seen that compared with the traditional closed-loop EKF, the closed-loop EKF-MMDE shows 64% and 62% improvement for the Mars explorer's position and velocity, respectively. The closed-loop EKF-MMDE has an approximately 11% increase in calculation time compared with the traditional one. For one step, the computation time of closed-loop EKF-MMDE increases by 11·6 us. This value is negligible compared with the filtering period of several hundred seconds. The reason is that the closed-loop EKF-MMDE uses the TOA measurement model considering the Doppler effects, and the computational load of the closed-loop EKF-MMDE is more than that of the closed-loop EKF by only one matrix $\boldsymbol{S}$ computation and two matrix accumulations. From these results, we can see that the closed-loop EKF-MMDE improves the navigation performance obviously under the condition of the Doppler effects.

Next, we investigate the impact of the X-ray sensor's area on both the closed-loop EKF-MMDE and the traditional closed-loop EKF. Figure 4 represents the simulation results with different areas of sensor over 100 Montè-Carlo trials. We can

https://doi.org/10.1017/S0373463314000216 Published online by Cambridge University Press

Table 5. Comparison between the traditional closed-loop EKF and the closed-loop EKF-MMDE.

Filter	Position error/m	Velocity error/(m/s)	Total Time(s)	Time for each step(us)
closed-loop EKF	10291	4·156	0·095	109·8
closed-loop EKF-MMDE	3723	1·595	0·105	121·4

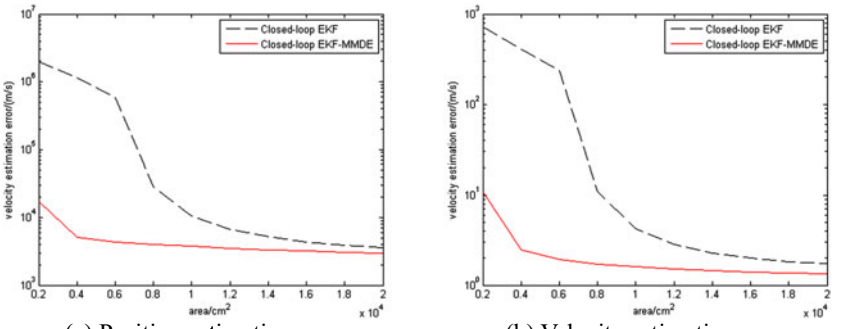

(a) Position estimation error (b) Velocity estimation error

Figure 4. Estimation error with different area of X-ray sensor.

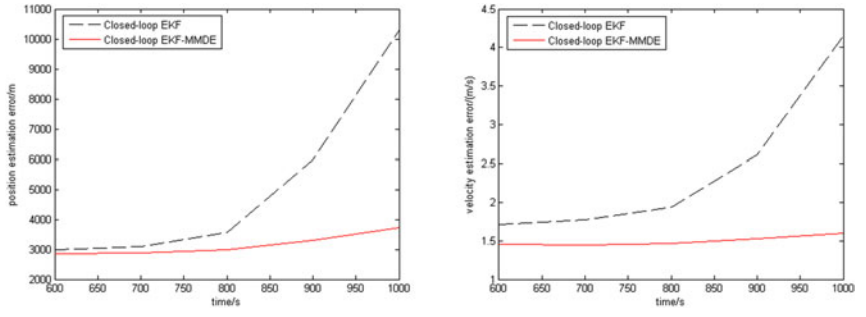

(a) Position estimation error (b) Velocity estimation error

Figure 5. Estimation error with different observation period.

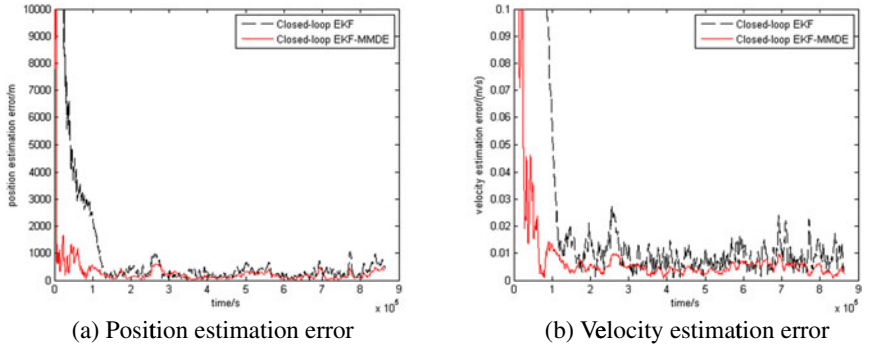

(a) Position estimation error (b) Velocity estimation error

Figure 6. Estimation error of the two navigation methods.

https://doi.org/10.1017/S0373463314000216 Published online by Cambridge University Press

Table 6. Comparison between the traditional EKF and the EKF-MMDE.

Filter	Position error/m	Velocity error/(m/s)	Total Time(s)	Time for each step(us)
Closed-loop EKF	359	0·0105	0·073	84·5
Closed-loop EKF-MMDE	269	0·0052	0·073	84·5

see that the performance of the two methods improves with enlarging the area of X-ray sensor, and the closed-loop EKF-MMDE method outperforms the traditional one with the same area. It is interesting to note that when the two methods reach the same accuracy, the area adopted by the closed-loop EKF-MMDE-based navigation is less than that of closed-loop EKF-based one. For instance, in order to reach 6000 m, the closed-loop EKF-MMDE-based navigation requires three X-ray sensors with $3 \times 4000\,\mathrm{cm}^2$ area, while the traditional closed-loop EKF-based method needs three X-ray sensors with $3 \times 13000\,\mathrm{cm}^2$. The novel closed-loop EKF-based navigation method saves $3 \times 9000\,\mathrm{cm}^2$ and decreases the cost and the weight of the Mars explorer effectively.

Finally, we investigate the impact of the filtering period on both the novel closed-loop EKF-MMDE and the traditional closed-loop EKF method. Figure 5 represents the simulation results with different filtering periods over 100 Montè-Carlo trials. We can see that the accuracy of the traditional closed-loop EKF declines with the increase of filtering periods greatly, while the accuracy variation of closed-loop EKF-MMDE is very small. The closed-loop EKF-MMDE method outperforms the traditional one with the same observation period. The reason is that with the increase of observation period, the TOA bias increases, the traditional closed-loop EKF cannot resist the TOA bias, while the closed-loop EKF-MMDE is robust to the TOA bias.

When the X-ray sensor with small area is adopted, the number of received X-ray photons per unit time decreases greatly. In order to obtain high SNR pulsar profile, the pulsar signals observation period must be lengthened. Under this condition, the closed-loop EKF-MMDE works very well, while the closed-loop EKF does not. In brief, the closed-loop EKF-MMDE is well suited for small-area X-ray sensors.

5.2. *Earth-Mars transfer obit*. In this section, we investigate the performance of the closed-loop EKF and the traditional EKF in the Earth-Mars transfer orbit. When we choose $\boldsymbol{Q}$ as the state process noise covariance of the traditional EKF, the EKF cannot converge very well. The reason is that the EKF performance is affected by the correlated TOA measurement noise. Therefore, we should choose a larger $\boldsymbol{Q}$. From a lot of simulation results, we find that when a $\boldsymbol{Q}$ of 25 is adopted, the EKF can converge very well and the estimation accuracy is high. Figure 6 shows the performance comparison of these two navigation methods using the same simulation conditions described above. As the results in Figure 6 demonstrate, the two methods can converge very well, and the closed-loop EKF-MMDE performs considerably better. Table 6 shows the comparison between the traditional EKF and the EKF-MMDE over 100 Montè-Carlo trials. It can be seen that compared with the traditional closed-loop EKF, the closed-loop EKF-MMDE shows 35% and 50% improvement for the Mars explorer's position and velocity, respectively. The closed-loop EKF-MMDE has the same calculation time as the traditional closed-loop EKF.

https://doi.org/10.1017/S0373463314000216 Published online by Cambridge University Press

The reason is that the closed-loop EKF-MMDE can deal with the influence of Doppler effects very well via the improvement of measurement model. In the transfer orbit, the simplified measurement model is adopted, which does not increase the computational load.

6. CONCLUSION. In this paper, pulsar navigation for the Mars explorer resistant against Doppler effects is proposed. In the pulsar signals observation period, the Doppler velocity predicted by the orbit dynamic model and the prior information is utilized to compensate the X-ray photon time-of-arrival. However, there is a bias caused by the Doppler compensation in the TOA estimation, and the bias is correlated with the state estimation error. To solve this problem, we build the TOA measurement model with the Doppler effects, and utilise the closed-loop EKF-MMDE as the navigation filter. Compared with the traditional closed-loop EKF, the closed-loop EKF-MMDE clearly improves the navigation performance with a negligible computational load.

This X-ray pulsar navigation system has the following virtues: (1) navigation is completely autonomous; (2) it is able to resist the Doppler effects and has high accuracy; (3) it realizes real-time Doppler compensation and state estimation; (4) it works very well with a small-area X-ray sensor. Therefore, this pulsar navigation system is suited for Mars exploration.

ACKNOWLEDGEMENTS

This work was supported by the State Key Program of National Natural Science of China (grant number 61233005), Specialized Research Fund for the Doctoral Program of Higher Education (grant number 20124219120002), Scientific Research Program Funded by Hubei Provincial Education Department (grant number Q20131110) and Natural Science Foundation of Hubei Province of China (grant number 2013CFB333).

REFERENCES

Ashby, N. and Golshan, R. (2008). Minimum uncertainties in position and velocity determination using X-ray photons from millisecond pulsars. *Proceedings of ION NTM 2008*, San Diego, CA.

Dennis, W.W. (2005). The use of X-ray pulsars for aiding GPS satellite orbit determination. Master dissertation, Air Force Institute of Technology.

Emadzadeh, A.A. and Speyer, J.L. (2011a). X-ray pulsar-based relative navigation using epoch folding. *IEEE transactions on Aerospace and Electronic Systems*, **47**, 2317–2328.

Emadzadeh, A.A. and Speyer, J.L. (2011b). Relative navigation between two spacecraft using X-ray pulsars. *IEEE Transactions on Control Systems Technology*, **19**, 1021–1035.

Fei, B.L., Pan, G.T. and Yao, G.Z. (2011a). Arithmetic of frequency drift and time delay between pulse profiles in XNAV. *Acta Geodaeticaet Cartographica Sinica*, **40**, 126–132.

Fei, B.J., Yao, G.Z., Du, J. and Sun, W.J. (2011b).The pulse profile and united measurement equation in XNAV. *Science China: Physics, Mechanics & Astronomy*, **40**, 644–650.

Golshan, R. and Sheikh, S. (2008). On pulse phase estimation and tracking of variable celestial X-ray sources. *Proceedings of the Institute of Navigation*, San Diego, CA.

Li, J.X. and Ke, X.Z. (2011). Maximum-likelihood TOA estimation of x-ray pulsar signals on the basis of poison model. *Chinese Astronomy and Astrophysic*, **35**, 19–28.

Liu, J., Ma, J. and Tian, J.W. (2010). CNS/pulsar integrated navigation using two-level filter. *Chinese Journal of Electronics*, **19**, 265–269.

Liu, J., Ma, J., Tian, J.W., Kang, Z.W. and White, P. (2012). Pulsar navigation for interplanetary missions using CV model and ASUKF. *Aerospace Science and Technology*, **22**, 19–23.

Ning, X.L., Ma, X., Peng, C., Quan, W., and Fang, J.C. (2012). Analysis of filtering methods for satellite autonomous orbit determination using celestial and geomagnetic measurement. *Mathematical Problems in Engineering*, 2012, 267875.

Ning, X.L., Wang, L.H., Wu, W.R., and Fang, J.C. (2011). A celestial assisted INS initialization method for lunar explorers. *Sensors*, **11**, 6991–7003.

Qiao, L., Liu, J.Y., Zheng, G.L., Xiong, Z. (2010). Closed-loop filter design for X-ray pulsar-based satellite navigation system. *Control Theory and Application*, **27**, 939–947.

Rinauro, S., Colonnese, S. and Scarano, G. (2013). Fast near-maximum likelihood phase estimation of X-ray pulsars. *Signal Processing*, **93**, 326–331.

Sheikh, S.I., Pines, D.J. and Ray, P.S. (2006). Spacecraft navigation using x-ray pulsars. *Journal of Guidance, Control and Dynamics*, **29**, 49–63.

Xie, Q., Xu, L.P., Zhang, H. and Luo, N. (2012). Doppler estimation of X-ray pulsar signals based on profile feature. *Journal of Astronautics*, **33**, 1301–1307.

Xiong, K., Wei, C.L. and Liu, L.D. (2013). Autonomous navigation for a group of satellites with star sensors and inter-satellite links. *Acta Astronautica*, **86**, 10–23.

Xu, W.M., Cui, H.T., Cui, P.Y. and Liu, Y.F. (2007). Selection and planning of asteroids for deep space autonomous optical navigation. *Acta Aeronauticaet Astronautica Sinica*, **28**, 891–896.

Zhang, H., Xu, L.P. and Xie, Q.H. (2011). Modeling and Doppler measurement of X-ray pulsar. *Science China*: *Physics, Mechanics & Astronomy*, **54**, 1068–1076.

Zhang, X.W., Wang, D.Y. and Huang, X. Y. (2009). Study on the selection of the beacon asteroids in autonomous optical navigation for interplanetary exploration. *Journal of Astronautics*, **30**, 947–952.